2D and 3D Silver-Based Coordination Polymers with Thiomorpholine-4-carbonitrile and Piperazine-1,4-dicarbonitrile: Structure, Intermolecular Interactions, Photocatalysis, and Thermal Behavior

Predrag Ristić[a], Nenad Filipović[b], Vladimir Blagojević[c], Jovana Ćirković[d], Berta Barta Holló[e], Veljko Đokić[f], Morgan Donnard[g], Mihaela Gulea[h], Ivana Marjanović[e], Olivera R. Klisurić[e], Tamara R. Todorović[a*]

[a]University of Belgrade - Faculty of Chemistry, Studentski trg 12-16, 11000 Belgrade, Serbia

[b]University of Belgrade, Faculty of Agriculture, Nemanjina 6, 11000 Belgrade, Serbia

[c]Institute of Technical Sciences of the Serbian Academy of Sciences and Arts, Knez Mihailova 35/IV, 11000   Belgrade, Serbia

[d]University of Belgrade, Institute for Multidisciplinary Research, Kneza Višeslava 1, 11030 Belgrade, Serbia

[e]University of Novi Sad, Faculty of Sciences, Trg Dositeja Obradovića 3, 21000 Novi Sad, Serbia

[f]Innovation Center of Faculty of Technology and Metallurgy in Belgrade Ltd, Belgrade, Serbia

[f]Université de Strasbourg, Université de Haute-Alsace, CNRS, LIMA-UMR 7042, ECPM, 67000 Strasbourg, France

[g]Université de Strasbourg, CNRS, LIT-UMR 7200, Faculty of Pharmacy, 67000 Strasbourg, France

*Corresponding author:

Tamara R. Todorović, PhD, Associate Professor, University of Belgrade - Faculty of Chemistry, Studentski trg 12-16, 11000 Belgrade, Serbia; E-mail: tamarat@chem.bg.ac.rs

Abstract

Four silver-based coordination polymers $\{[Ag(L1)_2]NO_3\}_\infty$ (**1**), $\{[Ag(L1)_2]ClO_4\}_\infty$ (**2**), $\{[Ag(L2)_2]NO_3 \cdot H_2O\}_\infty$ (**3**) and $\{[Ag(L2)_2]ClO_4\}_\infty$ (**4**) were synthesized using thiomorpholine-4-carbonitrile (L1) and piperazine-1,4-dicarbonitrile (L2) ligands. Compounds **1** and **2** are two-dimensional, while **3** and **4** are three-dimensional. L1 and L2 are 1,4–bis-monodentate ligands in all compounds, while Ag(I) ions are four-coordinated in a slightly distorted tetrahedral geometry. Topological analysis in standard representations suggests that underlying nets in **1** and **2** have a **sql**, while **3** and **4** exhibit **dia** topology. Thermal analysis shows that **3** loses crystalline water at room temperature, while other compounds show good thermal stability. All compounds show good photocatalytic activity for photocatalytic degradation of mordant blue 9 dye, with reaction rates in the range 0.029 to 0.061 min^{-1}. The best result was obtained for compound **4**, which can be correlated to its largest lattice volume.

Keywords: Silver complexes; Coordination polymers; Topology; Thermal stability; Photocatalysis.

Introduction

In recent years, coordination polymers (CPs) have become increasingly important in material science. Due to their structural diversity,[1] they have a wide application such as drug delivery, gas storage, catalysis, luminescence, redox-active materials for carbon-based electrodes, removal of pollutants from the environment, etc.[2–5] Also, these materials have potential application as antibacterial agents[6,7] and high-performance supercapacitors.[8] The combination of cations of 3d and 4f-transition metals can lead to the creation of multifunctional and multidimensional hetero-metalorganic frameworks which may have photocatalytic, magnetic and combined properties simultaneously.[9–11]

Analysis of the data deposited in the Cambridge Structural Database[12] revealed that 8 % of all CPs in MOFs subset are Ag-CPs. Silver as a metal of choice for construction of CPs provides a great diversity in coordination numbers (2-6 and even higher), as well as different types of interactions (Ag⋯ligand, Ag⋯π, Ag⋯Ag, Ag⋯C, C–H⋯π, π–π stacking and classical H-interactions) that lead to the creation of self-assembled supramolecular structures.[13, Dalton Trans., 2011, 40, 1224-1226, Inorg. Chem., 2013, 52, 5914-5923] Also, the structures of Ag-CPs

are influenced by the anion type of silver salt used for their synthesis. Some topologies of 2D Ag-CPs are **sql**, **hcb** and **fes**[14–18] while 3D topologies like **pcu**, **ths**, **pts, sra** and **irl** are observed.[19–22 Cryst. Growth Des., 2019, 19, 2235]

2D Ag-CPs can show potential application as photocatalysts,[23, Cryst. Growth Des., 2020, 20, 1130] luminescent[24, CrystEngComm, 2021, 23, 56, Dalton Trans., 2015, 44, 5837-5847] and nanomaterials.[25] Also, 2D Ag-CPs can be designed to show detonation performance,[26] sorption and selectivity to certain ions.[27] One of the most significant applications of insoluble coordination polymers is in heterogeneous catalysis because the catalyst can be easily separated and regenerated from the reaction mixture. There were several reports on Ag-CPs manifesting excellent catalytic and photocatalytic properties.[23,28,29] One of the significant applications of photocatalytically active coordination polymers is the oxidation of organic pollutants such as tartrazine, rhodamine B, and 2,4-dichlorophenol in natural watercourses.[28] Additionally, 2D Ag-CPs show biological potential as antibacterial agents[30] and as cytotoxic agents against breast and colon cancers.[31]

The potential application of 3D Ag-CPs is very similar to 2D Ag-CPs. Due to their properties, 3D Ag-CPs have potential application as photoluminescence materials,[32, Inorg. Chem. 2021, 60, 4375−4379] in an anion exchange, guest inclusion and electrochemical measurements,[33] as well as in modern electronic devices as supercapacitors.[8,34] Also, a highly efficient Ag-MOF based electrochemical sensor, capable of detecting ultra-trace penicillin, was fabricated.[35]

In our previous work[13] we synthesized four Ag-CPs with thiomorpholine-4-carbonitrile and aromatic polyoxoacids as co-ligands. We showed that all of them have good thermal stability and reasonable reaction rates in the photocatalytic degradation of mordant blue 9 (MB9) dye, while two of them showed luminescent properties. As a continuation of our previous work on Ag-CPs we performed the synthesis of new Ag-based 2D and 3D CPs, their characterization, crystallographic analysis of intermolecular interactions, investigation of photocatalytic properties and thermogravimetric analysis. To improve the photocatalytic properties, two ligands with related cyclic cyanamide structures were used to obtain new Ag-CPs: the previously reported thiomorpholine-4-carbonitrile (L1) and the newly investigated piperazine-1,4-dicarbonitrile (L2).

Experimental

Materials and methods

All the employed reagents and solvents were of analytical grade and used without further purification. $AgNO_3$ ($\geq$ 99.0 %) and anhydrous $AgClO_4$ (97 %) were obtained from Sigma-Aldrich (Sigma-Aldrich Chemie GmbH, Steinheim, Germany). Elemental analyses (C, H, N, S) were performed by the standard micro-methods using the ELEMENTARVario ELIII C.H.N.S=O analyser. Infra-red (IR) spectra were recorded on a Thermo Scientific Nicolet 6700 FT-IR spectrometer by the Attenuated Total Reflection (ATR) technique in the region 4000−400 cm^{-1}. Abbreviations used for IR spectra: vs, very strong; s, strong; m, medium; w, weak. Solid state diffuse reflectance UV-Vis spectra were recorded using an Agilent Cary 5000 UV-Vis-NIR spectrophotometer, equipped with an integrating sphere. Data were collected from 200 to 800 nm, with scan rate 600 nm/min and data interval of 1 nm. A commercial PTFE cell was used as reference.

Synthesis of the ligand thiomorpholine-4-carbonitrile (L1)

The ligand was synthesized according to our previously reported procedure.[13] In a round bottom flask, thiomorpholine (103 mg, 1 mmol), acetonitrile (0.5 mol dm^{-3}, 2 mL) and tetramethylethylenediamine (232 mg, 2 mmol) were mixed. Then CuCN (179 mg, 2 mmol) was added and the mixture was flushed with oxygen. The reaction solution was then let to stir under 1 atmosphere of O_2 for 18 h. After a short filtration over Celite® that was rinsed thrice with AcOEt (3 × 3 mL), the crude mixture was concentrated under vacuum and purified by flash column chromatography (Pentane/AcOEt, SiO_2) to afford the entitled product. Yield 0.12 g (94%). White solid; m.p.: 41–43 °C. Anal. Calcd. for $C_5H_8N_2S$ (MW = 128.19): C, 46.85; H, 6.29; N, 21.85; S 25.01 %. Found: C, 46.65; H, 6.73; N, 21.74; S 25.12 %. ATR-FTIR (cm^{-1}): 2961 (w), 2921 (w) and 2863 (w) (Csp^3–H); 2210 (vs) (C≡N). ^{1}H NMR (CDCl$_3$, 500 MHz) δ 2.70 (t, J = 5.1 Hz, 4H), 3.46 (t, J = 5.1 Hz, 4H); ^{13}C NMR (CDCl$_3$, 126 MHz) δ 26.1 (2C), 50.8 (2C), 117.4.

Synthesis of the ligand piperazine-1,4-dicarbonitrile (L2)

A solution of sodium hydrogen carbonate (3.9 g, 46.44 mmol) in H_2O (10 mL) was slowly added to a stirred solution of piperazine (1 g, 11.6 mmol) in dichloromethane (25 mL) at 0°C. A solution of cyanogen bromide (2.58 g, 24.38 mmol) in dichloromethane (10 mL)

was then added to the reaction mixture at 0°C. The mixture was stirred at 0°C for 30 minutes, then allowed to rise to ambient temperature and stirred for an additional 2 hours. Finally, the layers were separated, the dichloromethane phase was washed with aqueous saturated $NaHCO_3$ solution (25 mL), brine (25 mL), dried over $MgSO_4$ and evaporated in vacuo to obtain an off white solid. The desired compound was obtained in 75% yield (1.18 g, 8.67 mmol) as a white solid after recrystallization from EtOH, m.p.: 165–167 °C. ^{1}H NMR ($CDCl_3$, 500 MHz) δ 3.32 (s, 8H); ^{13}C NMR ($CDCl_3$, 126 MHz) δ 47.2 (4C), 117.4 (2C).

Synthesis of {[Ag(L1)$_2$]NO$_3$}$_\infty$ (1) and {[Ag(L1)$_2$]ClO$_4$}$_\infty$ (2)

1: $AgNO_3$ (0.033 g, 1.95×10^{-4} mol) was added into the solution of L1 (0.050 g, 3.9×10^{-4} mol) in H_2O (5 mL). Reaction mixture in amber round bottom flask was refluxed for 1 h. Colorless solution was left and kept away from light for 5 days. White crystals were separated by filtration and dried in desiccator. Yield: 0.027 g (32.50 %). Anal. calcd. for $C_{10}H_{16}AgN_5S_2O_3$ (MW = 426.27): C, 28.18; H, 3.78; N, 16.43; S, 15.04. Found: C, 28.05; H, 3.82; N, 16.24; S, 14.99. ATR-FTIR (cm^{-1}): 2972 (w) and 2924 (w) (Csp^3–H); 2222 (vs) (C≡N); 1362 (vs) and 1343 (vs) (N–O nitrate).

2: The complex was synthesized in a similar way to **1**, but using $AgClO_4$ (0.044 g, 1.95×10^{-4} mol) instead of $AgNO_3$. Yield: 0.045 g (49.71 %). Anal. Calcd. for $C_{10}H_{16}AgClN_4O_4S_2$ (MW = 463.71): C, 25.90; H, 3.48; N, 12.08; S, 13.83. Found: C, 25.89; H, 3.21; N, 12.04; S, 13.78. ATR-FTIR (cm^{-1}): 2997 (w) and 2927 (w) (Csp^3–H); 2226 (vs) (C≡N); 1106 (vs) and 1083 (vs) (Cl–O perchlorate).

Synthesis of {[Ag(L2)$_2$]NO$_3$· H$_2$O}$_\infty$ (3) and {[Ag(L2)$_2$]ClO$_4$}$_\infty$ (4)

3: The solid $AgNO_3$ (0.012 g, 7.34×10^{-5} mol) was added into the solution of L2 (0.020 g, $1.46 \cdot 10^{-4}$ mol) in EtOH (10 mL). Reaction mixture in amber round bottom flask was refluxed for 1 h. Colorless solution was left and kept away from light for 3 days. After 3 days, colorless single crystals suitable for X-ray diffraction analysis, were obtained by slow evaporation, separated by filtration and dried in desiccator. Yield: 0.019 g (10.62 %). Anal. Calcd. for $C_{12}H_{18}AgN_9O_4$ (MW = 460.22): C, 31.32; H, 3.99; N, 27.39. Found: C, 31.39; H, 3.71; N, 27.69. ATR-FTIR (cm^{-1}): 3010 (w) and 2938 (w) (Csp^3–H); 2229 (vs) (C≡N); 1381 (s) and 1338 (s) (N–O nitrate).

4: The solid $AgClO_4$ (0.025 g, 1.21×10^{-4} mol) was added into the solution of L2 (0.020 g, 1.46×10^{-4} mol) in H_2O (10 mL). Reaction mixture in amber round bottom flask

was refluxed for 90 min. Colorless solution was left and kept away from light for 5 days. Colorless single crystals were separated by filtration and dried in desiccator. Yield: 0.007 g (12.11 %) Anal. calcd. for $C_{12}H_{16}AgClN_8O_4$ (MW = 479.65): C, 31.05; H, 3.36; N, 23.36. Found: C, 30.96; H, 3.20; N, 23.31. ATR-FTIR (cm^{-1}): 2941 (w) and 2875 (w) (Csp^3–H); 2232 (vs) (C≡N); 1087 (s) (Cl–O perchlorate).

X-ray crystallography

X-ray diffraction data for **1**–**4** were collected at room temperature on a Rigaku (Oxford Diffraction) Gemini S diffractometer. CrysAlisPro and CrysAlis RED software packages[36] were used for data collection and data integration. Space group determinations were based on analysis of the Laue class and systematically absent reflections. Collected data were corrected for absorption effects using analytical absorption correction for **1** and **3** and numerical absorption correction based on Gaussian integration for **2** and **4** applying a multifaceted crystal model.[37,??] (??:Coppens, P. (1970). In *Crystallographic Computing*, edited by F. R. Ahmed, S. R. Hall & C. P. Huber, pp. 255–270. Copenhagen: Munksgaard).Structure solution and refinement were carried out with the programs SHELXT[38] and SHELXL–2018/3,[39] respectively. Crystal structure of **3** was solved as a non-merohedral twin with a BASF factor value of 0.12. MERCURY[40] was employed for molecular graphics and WinGX[41] software was used to prepare material for publication. Non-hydrogen atoms in **1**–**4** were refined anisotropically. In **3**, H atoms were identified on difference electron density maps and isotropically refined, while H atoms in **4** were treated by a mixture of independent and constrained isotropic refinement H atoms. In **1** and **2** H atoms were treated by constrained isotropic refinement. Crystal data and refinement parameters for **1**–**4** are summarized in Table 1. Topological analysis was performed with the ToposPro program package and the Topological Types Database collection of periodic network topologies.[42]

Table 1. Crystallographic data and refinement parameters for **1**−**4**

Crystal data				
Compound	**1**	**2**	**3**	**4**
Chemical formula	$2(C_5H_8Ag_{0.50}N_2S)\cdot NO_3$	$2(C_5H_8Ag_{0.50}N_2S)\cdot ClO_4$	$C_{12}H_{18}AgN_9O_4$	$C_{12}H_{16}AgClN_8O_4$
M_W	426.27	463.71	460.22	479.65
Crystal system, space group	Tetragonal, $P\bar{4}2_1m$	Tetragonal, $P\bar{4}2_1m$	Triclinic, $P\bar{1}$	Orthorhombic, $Pnnn$
a (Å),	13.1512(5)	13.1198(3)	6.6706(4)	12.6128(3)
b (Å)	13.1512(5)	13.1198(3)	10.5894(9)	13.1579(3)
c (Å)	4.3773(3)	4.6860(2)	13.5484(11)	16.1737(3)
α (°)	90	90	91.104(7)	90
β (°)	90	90	99.965(5)	90
γ (°)	90	90	103.416(6)	90
V (Å^3)	757.07(8)	806.60(5)	915.10(12)	2684.15(10)
Z	2	2	2	6
D_x (Mg m^{-3})	1.870	1.909	1.670	1.780
Radiation type	Mo $K\alpha$ ($\lambda = 0.71073$ Å)	Cu $K\alpha$ ($\lambda = 1.54184$ Å)	Mo $K\alpha$ ($\lambda = 0.71073$ Å)	Cu $K\alpha$ ($\lambda = 1.54184$ Å)
μ (mm^{-1})	1.62	14.18	1.14	10.76
Crystal size (mm)	0.72 × 0.14 × 0.10	0.29 × 0.08 × 0.07	0.52 × 0.13 × 0.06	0.70 × 0.38 × 0.27
Data collection				
Absorption correction	Analytical	Gaussian	Analytical	Gaussian

T_{min}, T_{max}	0.858, 0.963	0.161, 0.462	0.765, 0.940	0.036, 0.200
Reflections collected	1705	1211	6839	16023
Independent reflections	837	711	6839	2641
Observed reflections [$I > 2\sigma(I)$]	730	654	5792	2088
R_{int}	0.022	0.025	0.020	0.028
θ values (°)	$\theta_{max} = 29.0$, $\theta_{min} = 3.5$	$\theta_{max} = 71.7$, $\theta_{min} = 4.8$	$\theta_{max} = 29.1$, $\theta_{min} = 3.1$	$\theta_{max} = 72.0$, $\theta_{min} = 4.3$
Refinement				
$R[F^2 > 2\sigma(F^2)]$, $wR(F^2)$	0.0284, 0.0532	0.0250, 0.0617	0.0425, 0.0978	0.0301, 0.0873
$R[all\ data]$, $wR2$	0.0373, 0.0580	0.0287, 0.0641	0.0528, 0.1048	0.0368, 0.0961
Goodness-of-fit (S)	1.043	1.057	1.096	1.052
No. of reflections	837	711	6839	2641
No. of parameters	77	60	308	196
No. of restraints	25	0	2	0
$\Delta\rho_{max}$, $\Delta\rho_{min}$ (e Å^{-3})	0.30, −0.53	0.23, −0.49	0.56, −0.51	0.65, −0.49
CCDC no.	2068533	2068534	2068535	2068536

The Powder X-ray diffraction (PXRD) experiment was conducted on a Rigaku Smartlab X-ray diffractometer in $\theta-\theta$ geometry (the sample in horizontal position) in parafocusing Bragg-Brentano geometry using D/teX Ultra 250 strip detector in 1D standard mode with CuKα1,2 radiation source ($U = 40$ kV and $I = 30$ mA). The PXRD patterns were collected in 5–65° 2θ range, with a step of 0.01°, and the data collection speed of 5 ° min^{-1} with horizontal sample rotation of 20 rpm. For every compound, a small amount of single-crystal sample was pulverized, and low background single crystal silicon sample holder was used to minimize the background. The crystal phases present in the samples were identified in dedicated Rigaku PDXL 2.0 software, comparing them with a user database comprised of CIFs previously obtained by a single crystal X-ray diffraction.

Hirshfeld surface analysis and intermolecular interaction energies

Hirshfeld surface analysis was carried out using the CIFs. Before calculating the surfaces, the lengths of the bonds which include hydrogen atoms were normalized to the standard values determined by neutron diffraction. The Hirshfeld surfaces visualization and the presentation of the results as d_{norm}, shape index, and curvedness and the calculation of 2D fingerprint plots with de and di distances were performed by Crystal Explorer v.17.5.[43,44] The parameter d_{norm} represents the sum of the distance of the nearest nucleus external to the surface (de) and the distance from the surface to the nearest nucleus internal to the surface (di), normalized by the van der Waals radius of the atom. The surfaces were mapped over a standard color scale, with the corresponding 2D fingerprint plots calculated using de and di values in the range 0.4–2.8 Å. The intermolecular interaction energies were determined using CrystalExplorer v17.5, with the wavefunction calculated using Gaussian09 software with the B3LYP method and DGDZVP basis set.[45] The model systems were built from supercells of different sizes by creating a non-polymeric system. This was achieved by removing the metal centers, preserving whole ligand molecules, and capping eliminated covalent bonds with hydrogen atoms to preserve the charge balance.

Photocatalytic and photophysical properties

Mordant blue 9 (MB9) is a commonly used dye in the textile industry and is a very common environmental pollutant. MB9 has not been widely investigated in much detail, so there

is a relative scarcity of publications investigating its degradation. A volume of 50 mL of dye solution (c = 0.05 mol dm^{-3}) in water was mixed with 50 mg of the tested complex. A complex powder was added to the water solution under constant stirring and left in the dark for 15 min to equilibrate. The sample was illuminated by a spotlight source (Hamamatsu LC5) from a distance of 1 cm (light intensity 5.2 mW cm^{-2}). The decomposition rate of MB9 as a function of irradiation time was measured by a Varian Cary 50 Scan UV-Vis spectrophotometer. Lamp with emission in UV and visible part of the spectrum is turned on, and 5 mL of solution was extracted at regular intervals and measured in UV/VIS spectrometer. MB9 has two main absorption regions: around 330 and around 530 nm. The relative concentration of MB9 is tracked using absorption intensities in these regions. Measured absorption intensities were used to calculate relative concentrations of MB9 dye and the corresponding rate constants for the photocatalytic degradation reaction of MB9 dye.[46] Dependence of $-\ln(C/C_0)$ on time, where the initial part of the curve shows linear dependence (with R-squared > 99%) in all four complexes, indicates that the reaction of the photocatalytic degradation of MB9 dye can be treated as a first-order reaction.

To investigate reusability, photodegradation experiment for complex **4** was repeated for three successive cycles. Particles of **4** were separated from the solution, centrifuged and washed with water prior to reuse for the next photodegradation cycle. Each photodegradation cycle was performed under the same conditions. The photodegradation efficiency (η) was calculated according to the following equation: $\eta = (1 - A_t/A_0) \times 100\%$, where A_0 denotes the initial absorbance of dye's solution and A_t denotes the absorbance of the dye after irradiation time in min. The photodegradation efficiency of the complexes after the first cycle was compared to titania (Degussa p25 titanium dioxide nanopowder, rutile : anatase / 85 : 15, 99.9%, 20 nm) under the same conditions.

To explore the possible photocatalytic mechanism of **4**, active species trapping experiments were performed. Ethanol (EtOH), benzoquinone (BQ), or ammonium oxalate (AO) were introduced as scavengers for hydroxyl radicals ($^\bullet$OH), superoxide ion ($^\bullet$O$_2^-$), and holes (h$^+$),[ref. Cryst. Growth Des. 2020, 20, 1130−1138] respectively. During the experiments, EtOH, BQ, or AO was added to the MB9 solution to obtain a concentration of 1 mM. Otherwise, the method was similar to the described experiment of photodegradation of the dye.

TGA-DSC-MS

Thermal data were collected using TA Instruments SDT Q600 thermal analyzer coupled to Hiden Analytical HPR20/QIC mass spectrometer. The decomposition was followed from room temperature to 500 °C at 10 °C min^{-1} heating rate in argon carrier gas (flow rate = 50 cm^3 min^{-1}). Sample holder/reference is alumina crucible/empty alumina crucible. The sample mass was 3–5 mg. Selected ions between m/z = 1–90 were monitored in multiple ion detection modes (MIDs).

Results and discussion

Molecular and crystal structures of 1–4

Coordination compounds **1** and **2** crystallize in the tetragonal $P\bar{4}2_1m$ space group. Complex cations consist of Ag atoms and L1 ligands, while anions are nitrate in **1** and perchlorate in **2**. In asymmetric units of **1** and **2**, Ag(I) ions are situated on a 2-fold axis along which two mirror planes intersect. Moreover, L1 lies on the (110) mirror plane with half-occupancy, except for the C2 and C3 atoms at general positions. The asymmetric unit of **1** contains an Ag(I) atom and a nitrate anion, both of a quarter occupancy, as well as half of the L1 ligand. All nitrate oxygen atoms (O1–O3) showed large displacement parameters. As they are located at a general position, the disordered atoms were flanked with PART -1 and PART 0. The asymmetric unit of **2** consists of an Ag(I) atom with a quarter occupancy, half of the L1 ligand and a perchlorate anion. The oxygen atoms belonging to the perchlorate anion are in a general position, while the occupancy of Cl1 is one quarter.

The molecular structures of **1** and **2**, illustrated in Figure 1, show that L1 ligands form a distorted tetrahedral geometry around Ag(I) atoms. The four-coordinated geometry indices τ_4[47] are 0.87 in **1** and 0.85 in **2**. Each of the Ag(I) in **1** and **2** is coordinated to two nitrogen and two sulphur atoms from four different L1 ligands. The selected bond lengths are given in Table 2. In **1** and **2**, molecules of L1 act as bridging ligands with *bis*–monodentate coordination modes connecting the Ag(I) atoms to form a two-dimensional coordination network (Figure 2). Topological analysis in the standard representation suggests that each Ag(I) atom acts as a 4-connected node and the overall structures **1** and **2** have a **sql** underlying net topology.[42] The

structures **1** and **2** comprise layers stacked along the *c*-axis with a thickness of 4.53 Å in **1** and 4.79 Å in **2** (Figure 2).
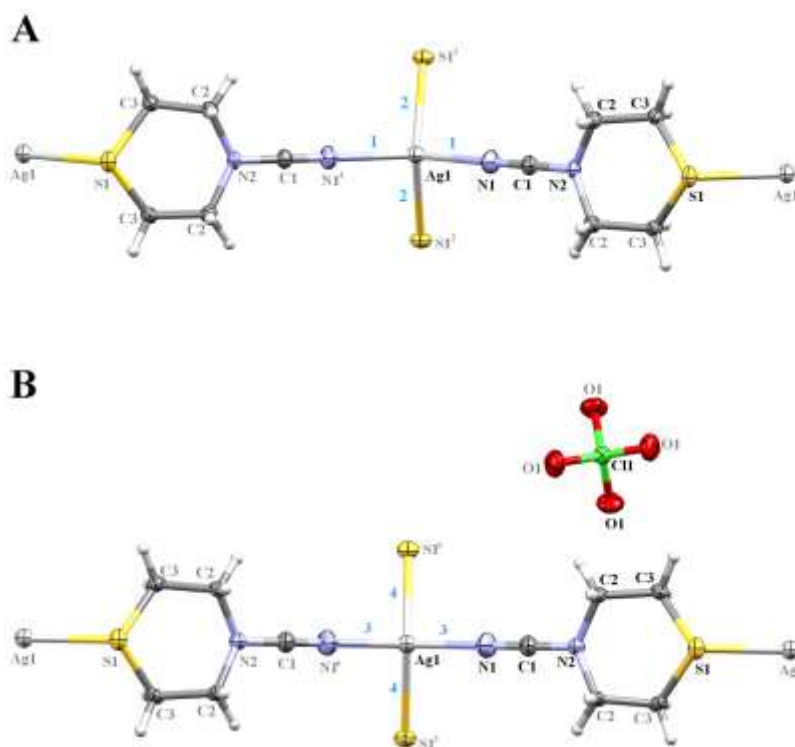

Figure 1. MERCURY[40] drawings of the molecular structure of compounds **1** (A) and **2** (B), with labeled non-H atoms. The atoms of the asymmetric unit are labeled in black. Displacement ellipsoids are shown at 30% probability level and H atoms are drawn as spheres of arbitrary radii. Disordered nitrate ion in **1** is omitted for clarity. Lengths of bonds (labelled as 1−4 in blue) are given in Table 2. Symmetry codes: (1) −*x*, −*y*+1, *z*; (2) *y*−1, −*x*+1, −*z*+1; (3) −*y*+1, *x*, −*z*+1; (4) −*x*+2, −*y*+1, *z*; (5) *y*+1, −*x*+1, −*z*+2; (6) −*y*+1, *x*, −*z*+2.
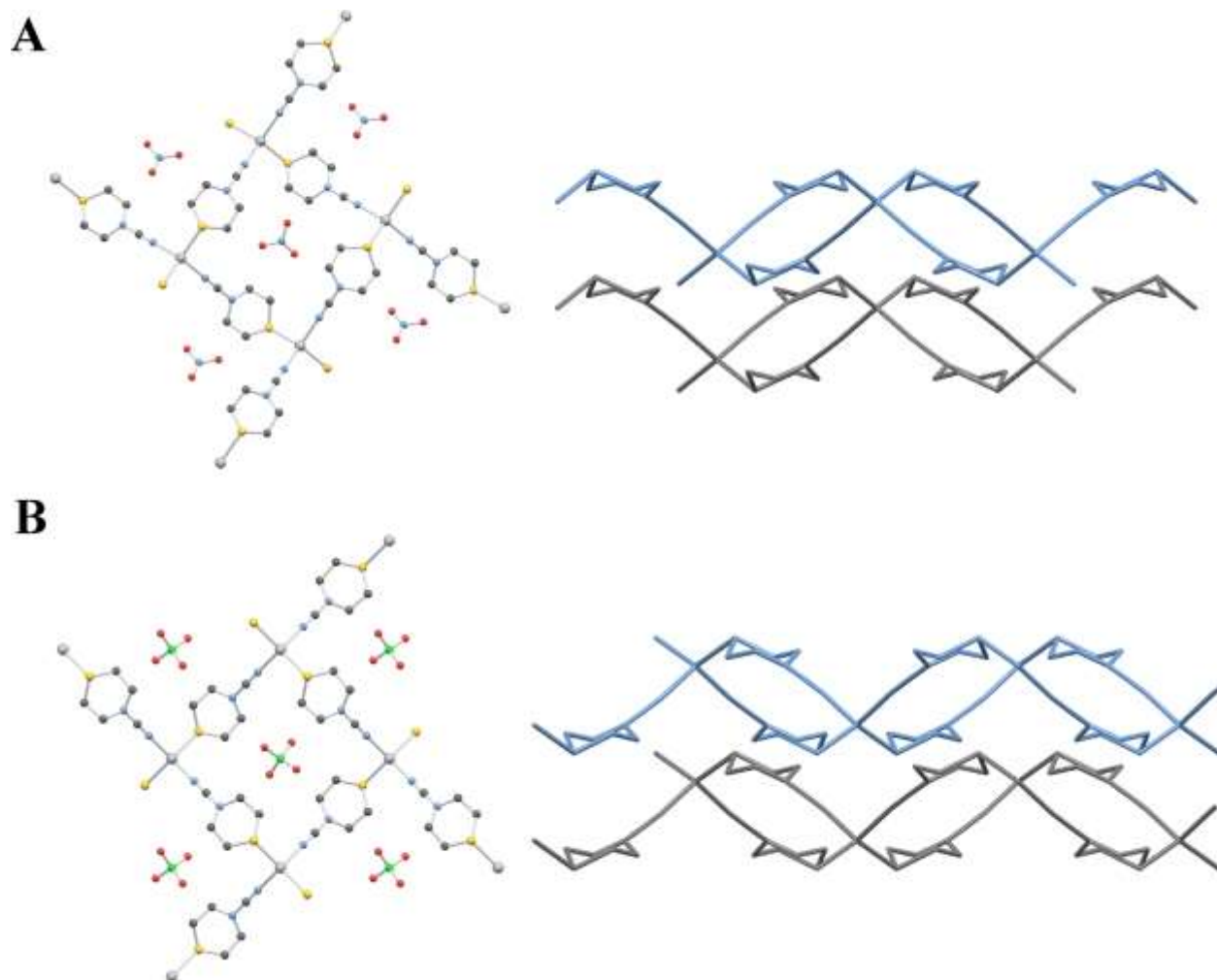
Figure 2. The packing in the crystal structures viewed along the *c*-axis (right) and stacked layers viewed along the *b*-axis (left) for compounds **1** (A) and **2** (B). All hydrogen atoms in presented extended layers are omitted for clarity.

Coordination compound **3** crystallizes in the triclinic $P\bar{1}$ space group, whereas compound **4** crystallizes in the orthorhombic *Pnnn* space group. Complex cations in these compounds consist of Ag (I) atoms and L2 ligands, while anions are nitrate in **3** and perchlorate in **4**. The asymmetric unit of **3** contains a single Ag(I) atom and four halves of the L2 ligands, one water guest molecule, and a nitrate anion. On the other hand, the asymmetric unit of **4** consists of two crystallographically different Ag(I) atoms, one and a half L2 ligand, and two independent perchlorate anions. The Ag1 ion is situated on a site with 222-symmetry (Wyckoff *a*) with half-occupancy, while Ag2 lies along a two-fold axis (Wyckoff *l*). The first perchlorate anion lies about a twofold axis with Cl1 at Wyckoff position 4*k*, whereas the half-occupancy Cl2 from the
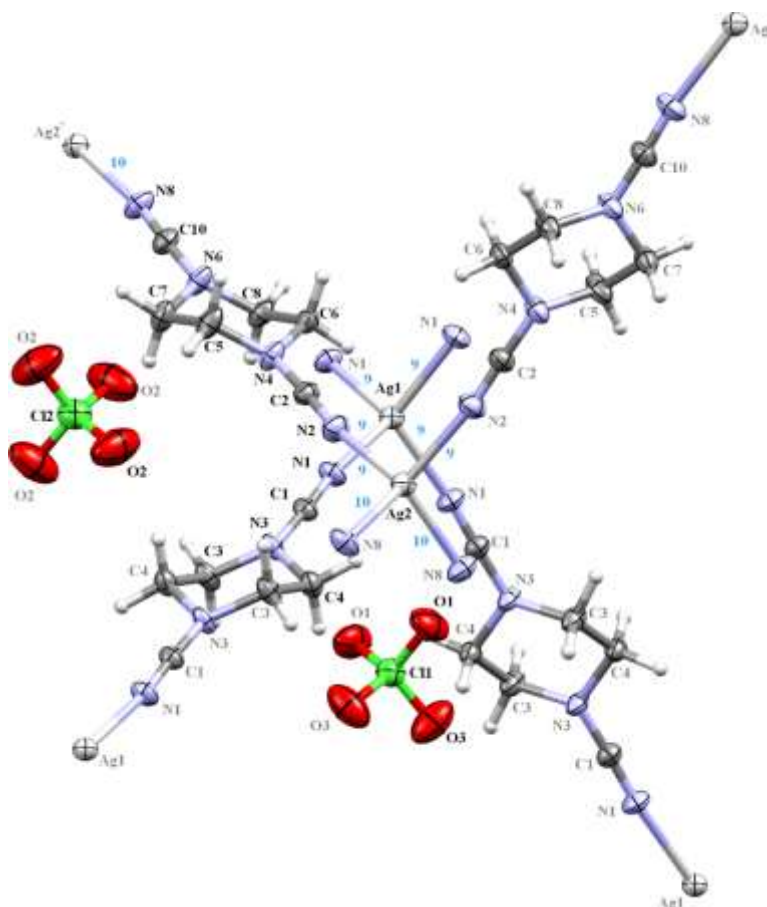
other perchlorate anion is situated on a 222-symmetry site (Wyckoff *b*). One-half of the L2 ligand coordinated to Ag1 *via* N1 lies on the axis containing the Cl1, while the L2 ligand coordinated to Ag2 *via* N2 lies about the axis containing the Ag2 ion.

The molecular structures of **3** and **4** shown in Figures 3 and 4 reveal that L2 ligands form a distorted tetrahedral geometry around Ag (I) atoms. The four-coordinated geometric index τ_4[47] is 0.92 in **3**. In **4**, the geometry indices τ_4[47] are 0.93 and 0.96 for the Ag1, and Ag2 environments, respectively. Each of the Ag(I) in **3** and **4** is coordinated to four nitrogen atoms from four different L2 ligands. The selected bond lengths are given in Table 2.

Figure 3. MERCURY[40] drawing of the molecular structure of **3**, with labeled non-H atoms. The atoms of the asymmetric unit are labeled in black. Displacement ellipsoids are shown at 30% probability level, and H atoms are drawn as spheres of arbitrary radii. Lengths of bonds (labelled as 5−8 in blue) are given in Table 2.

Figure 4. MERCURY[40] drawing of the molecular structure of **4**, with labeled non-H atoms. The atoms of the asymmetric unit are labeled in black. Displacement ellipsoids are shown at a 30% probability level, and H atoms are drawn as spheres of arbitrary radii. Lengths of bonds (labelled as 9 and 10 in blue) are given in Table 2. Symmetry code: (7) $x-1/2$, $-y+1$, $z+1/2$.

In **3** and **4**, the molecules of L2 act as bridging ligands with *bis*–monodentate coordination modes connecting the Ag(I) atoms to form three-dimensional coordination networks (Figures 5 and 6). In **3**, the Ag(I)…Ag(I) separations are 12.0168(12), 11.5727(11), 11.8866(12) and 12.1108(12) Å (Figure 3). On the other hand, the Ag(I)…Ag(I) separations in **4** are 12.1840(3) Å and 12.1840(4) Å for Ag1 and Ag2, respectively (Figure 4). Topological analysis in standard representation suggests that each Ag(I) atom acts as a 4-connected node, and the overall structures of **3** and **4** have a **dia** underlying net topology.[42] In **3**, the MOF structure comprises five interpenetrating networks (Figure 7) related by 6.67 Å translations along the [100] direction, thus being characterized by interpenetration class Ia.[48] The channels along the *a*–axis of the framework are occupied by hydrogen-bonded chains consisting of water molecules

15

and nitrate anions (Figure 5). Water molecules in **3** are connected by hydrogen bonds (Table S1). In **4**, the MOF structure comprises six interpenetrating networks (Figure 8), two of which are with Ag1 nodes related by 12.61 Å translations along the [100] direction (interpenetration class Ia).[48] The remaining four networks with Ag2 nodes are related both by 12.61 Å translations along the [100] direction and by an inversion centre (interpenetration class IIIa).[48]
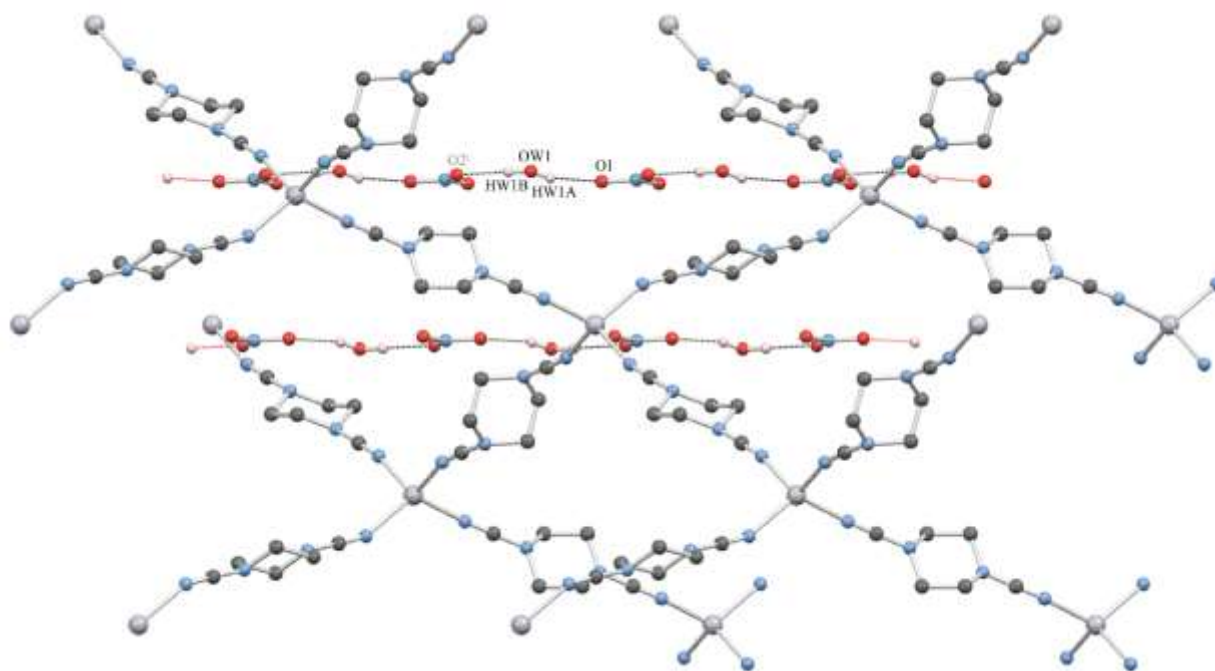

Figure 5. The crystal structure packing of **3** viewed along the *a*-axis. Selected hydrogen bonds are showed as dashed lines. Hydrogen atoms not involved in selected hydrogen bonds are omitted for clarity. Symmetry code: (i) $x-1, y, z$

Table 2. Selected bond lengths for **1−4**[a]

Compound	Bond label	Bond type	Bond length (Å)
1	1	Ag1–N1, Ag1–N1^1	2.324(6)
	2	Ag1–S1^2, Ag1–S1^3	2.5537(15)
2	3	Ag1–N1, Ag1–N1^4	2.317(7)
	4	Ag1–S1^5, Ag1–S1^6	2.5528(16)
3	5	Ag1–N1	2.269(4)

	6	Ag1–N2	2.257(5)
	7	Ag1–N3	2.256(4)
	8	Ag1–N4	2.248(5)
4	9	Ag1–N1, Ag2–N2	2.269(2)
	10	Ag2^7–N8	2.283(2)

^{a}Symmetry codes: (1) –x, 1–y, z; (2) 1–y, x, 1–z; (3) –1+y, 1–x, 1–z; (4) 2–x, 1–y, z; (5) 1+y, 1–x, 2–z; (6) 1–y, x, 2–z; (7) -½ + x, 1–y, ½ + z.
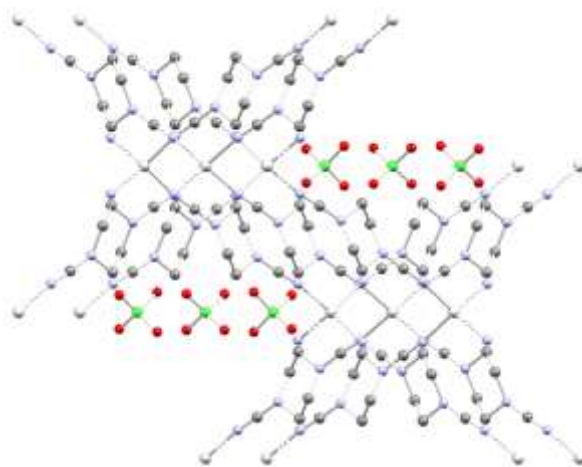
Figure 6. The crystal structure packing of **4** viewed along the *b*-axis. All hydrogen atoms are omitted for clarity.
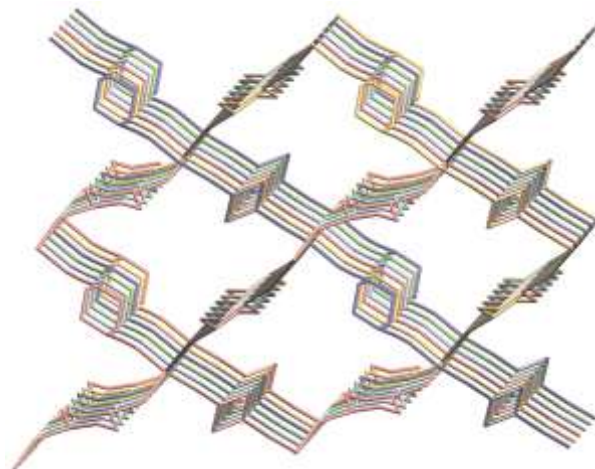
Figure 7. A schematic view of the five-fold interpenetration in **3**.
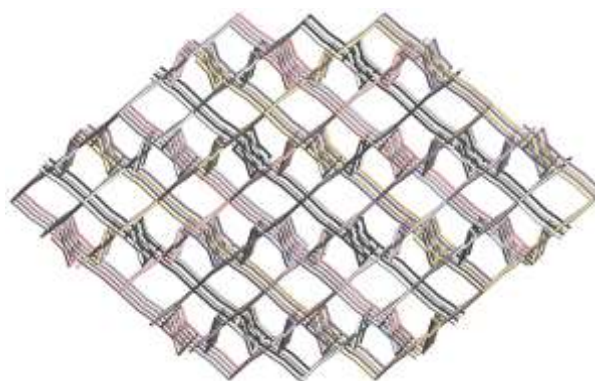
Figure 8. A schematic view of the six interpenetrating networks in **4**. Two Ag1 nets are given in black and white, while four Ag2 nets are in colour.

Powder X-ray diffraction analysis

All single crystal samples investigated by PXRD analysis represent single-phase systems (Figure 9). Since the second phase is absent, it can be concluded that the obtained single crystals are stable in the air under standard conditions and during pulverization.
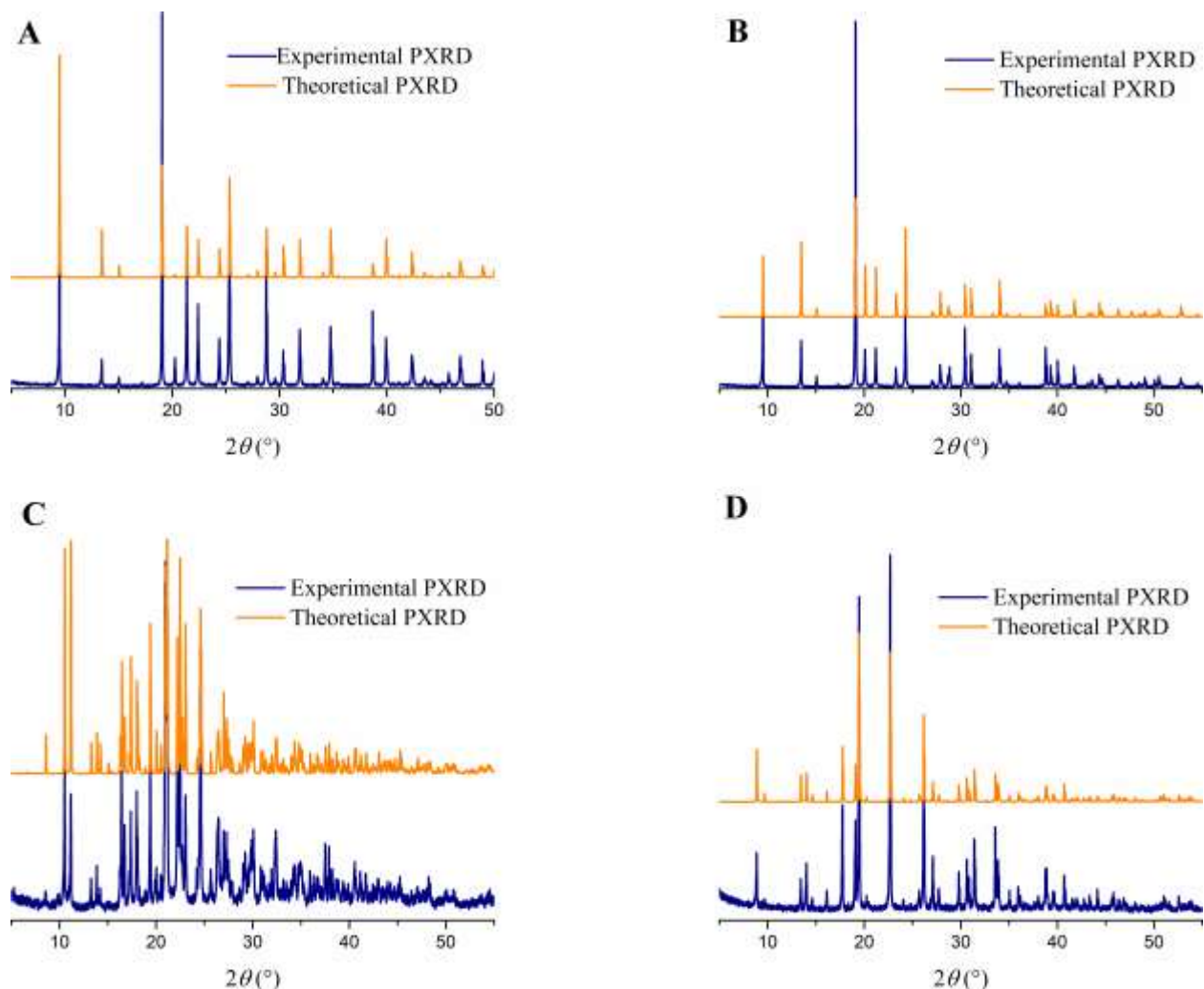
Figure 9. Experimental and theoretically obtained powder X-ray diffractograms of **1** (A), **2** (B), **3** **(C)** and **4** (D).

Hirshfeld and 2D fingerprint plot analysis

The Hirshfeld surface[49] a type of molecular surface, is often used to investigate, visualize and interpret all intra- and intermolecular interactions in a crystal structure. For better quantification of interactions, along with Hirshfeld surfaces, a 2D fingerprint plot is often used.[50] The Hirshfeld surfaces and the pseudosymmetric 2D fingerprint plots,[50] as well as the existing classical and non-classical interactions in the crystal structures of **1** and **2** are depicted in Figure 10. In complexes, interactions can be observed in the shape-index plot as red and blue regions, as well as in the curvature plot as a flat zone in the same position of the surface as in the shape-index plot. White circles mark the regions of the surfaces through which the complexes interact.
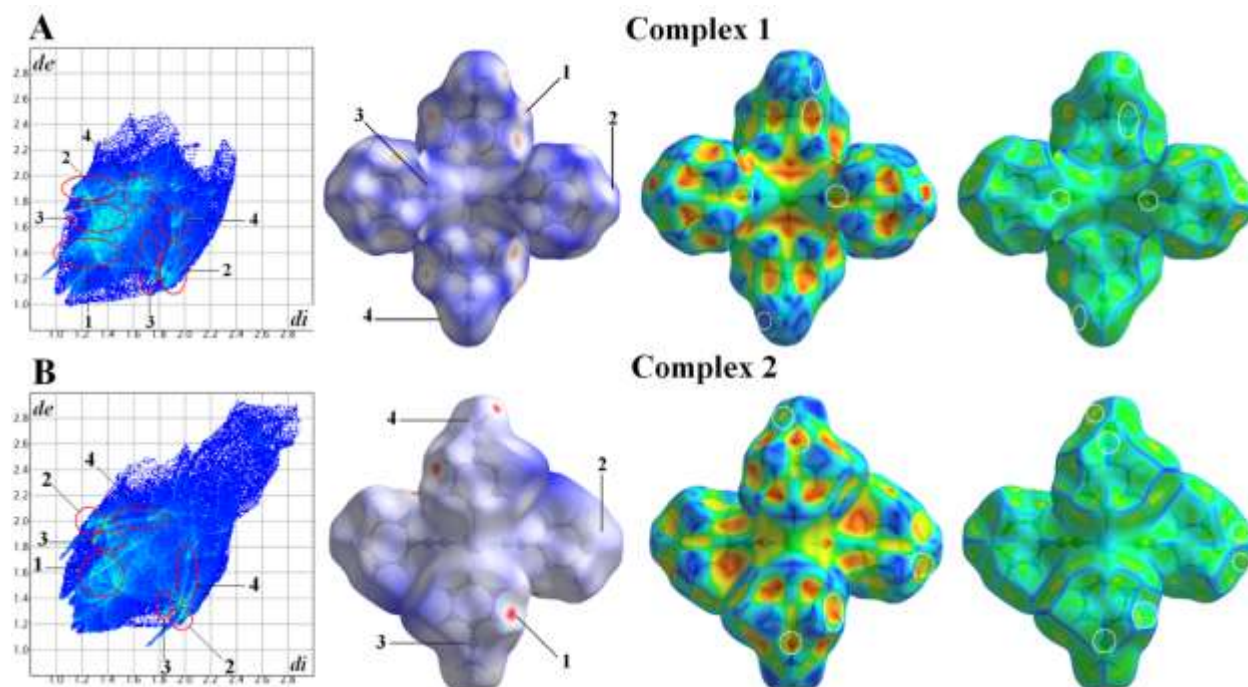
Figure 10. 2D fingerprint plot, Hirshfeld surface mapped with d$_{norm}$, shape index, and curvedness for **1** and **2**. For the interaction types, see Table 3.

Since complexes **1** and **2** are isostructural, it would probably be a good assumption to expect the same types of interactions, which is true. Generally, fingerprint plot analysis shows a trend that the percentage representation of all interactions, but the trend of the most engaged interactions differed. The relative contributions of different types of interactions in **1** and **2** are shown in Table 3. The O···H interactions are the most represented in **1**, while bifurcated S···H interactions, in which sulfur atom is a double proton acceptor, is the most represented in **2**. This trend is probably caused by the consequence of the difference between the anions of these two complexes. Analysis showed a trend that the percentage representation of all interactions in the crystal structure of **1** is greater than in **2**, which means that the representation of H···H contacts is higher in the crystal structure of **2**. Also, it was found that there were no interactions involving the central metal ion.

Table 3. Relative contributions and (di + de) values of different interaction types in the crystal structures of **1** and **2**.

Interaction number	Interaction type	1		2	
		relative contribution with included reciprocal contacts in %	di + de (Å)	relative contribution with included reciprocal contacts in %	di + de (Å)
1	O···H	18.2	2.42	10.8	2.46
2	S···H	13.2	2.82	12.8	2.76; 3.36
3	C···H	7.1	3.20	6.0	3.60
4	N···H	6.8	3.50	6.0	3.51

Intermolecular interactions

Since the results of the crystallographic analysis indicate that there are 2D networks in **1** and **2**, intermolecular energies were calculated for these two coordination polymers. Table 4 shows an overview of the calculated values of intermolecular interactions in model systems of these two complexes. Electronic interactions dominate in the structures of both complexes (Table 5), which can be related to the repulsive interactions that exist between the oxygen atoms of nitrate anions in **1** and perchlorate anions in **2**. Since the same trend of intermolecular interactions exists in **1** and **2**, the next most common is dispersion interactions which can be attributed to the stacking of 2D networks that result from the formation of classical and non-classical hydrogen interactions in the crystal packing of these polymers.[51] The difference in the values of dispersion interactions (–206.0 kJ mol^{-1} for **1** and –146.3 kJ mol^{-1} for **2**) stems from the presence of different anions in the crystal structures of these polymers. Also, this correlates with the distances between the 2D layers in **1** and **2** (4.377 Å for **1** and 4.686 Å for **2**) and with the fact that in **2** the S···H interactions are more represented in relation to O···H, while in **1** the trend is reversed.

Although **1** and **2** are isostructural, their structural differences contribute to polarization interactions, which differ by 10.5 kJ mol^{-1}. The relative contributions of these interactions are

the same (Table 5) in both cases. Still, the existence of an energy difference indicates the importance of qualitative structural differences and the geometric difference of the anions in the crystal structure of **1** and **2**. Qualitative differences and the orientation of donors and acceptors of hydrogen interactions are crucial for the existence of differences in the values and contributions of different types of intermolecular interactions.

Table 4. Overview of calculated values for intermolecular interactions (in kJ mol^{-1}) in model systems of **1** and **2**.

1				
Electron	Polarization	Dispersion	Repulsion	Total
564.90	−43.20	−206.00	129.60	445.30
2				
Electron	Polarization	Dispersion	Repulsion	Total
469.20	−32.70	−146.30	66.94	357.14

Table 5. Relative contributions (in %) to interactions in the crystal structures of **1** and **2**.

Complex	Electron	Polarization	Dispersion
1	59.86	4.58	21.83
2	65.61	4.57	20.46

UV-visible spectra and optical band gaps

The optical diffuse-reflection spectra for crystalline samples of **1−4** were measured at room temperature. With the assistance of the Kubelka−Munk function, the absorption (α/S) data were then calculated from the reflectance (Figure S1). All CPs showed absorption in the range 200−400 nm and have a pronounced peak around 230 nm, originating from the nitrile group common to both ligands. **1** and **3** exhibit a characteristic peak around 310 nm which can be correlated to the presence of the NO_3^- anion. The band gap energies (Eg) of **1–4** were obtained from the steep absorption edge (Figure S2). The Eg values for all CPs are similar (4.5−4.7 eV) and correspond to wide band gap semiconductors.

Photocatalytic properties

Photocatalytic properties were investigated in the reaction of photocatalytic degradation of MB9 dye (Figure 11). Since all complexes are insoluble in water, they were tested as heterogeneous catalysts in powder form for a degradation reaction in water. The progress of the degradation reaction was monitored using UV/VIS spectroscopy (Figure 12), and the results are shown in Table 6. Apparent first-order rate constants are in the 0.029 to 0.061 min^{-1} range, indicating good photocatalytic properties. This is comparable to or better than Ag-based coordination polymers' reported activities for photocatalytic degradation of organic dyes.[52–55] The lowest values were obtained for **2,** and the highest was obtained for **4**. Complexes **1** and **2** differ only in the counter-ion (NO_3^- and ClO_4^-, respectively). However, their rate constants show a considerable difference. This suggests that the oxygen from NO_3^- anion is probably more reactive since this would be expected to be the main reactive species. **3** exhibits similar photocatalytic activity as **1**, which can be correlated with the presence of the same NO_3^- anion. Structure. **4**, which contains ClO_4^-, shows the highest photocatalytic activity, which can be correlated to its larger lattice volume. Other compounds are more compact, so it is likely that **4** benefits from its less tightly packed structure, allowing faster penetration of dye molecules into the three-dimensional network.

Table 6. Calculated apparent first-order rate constants corresponding to each compound

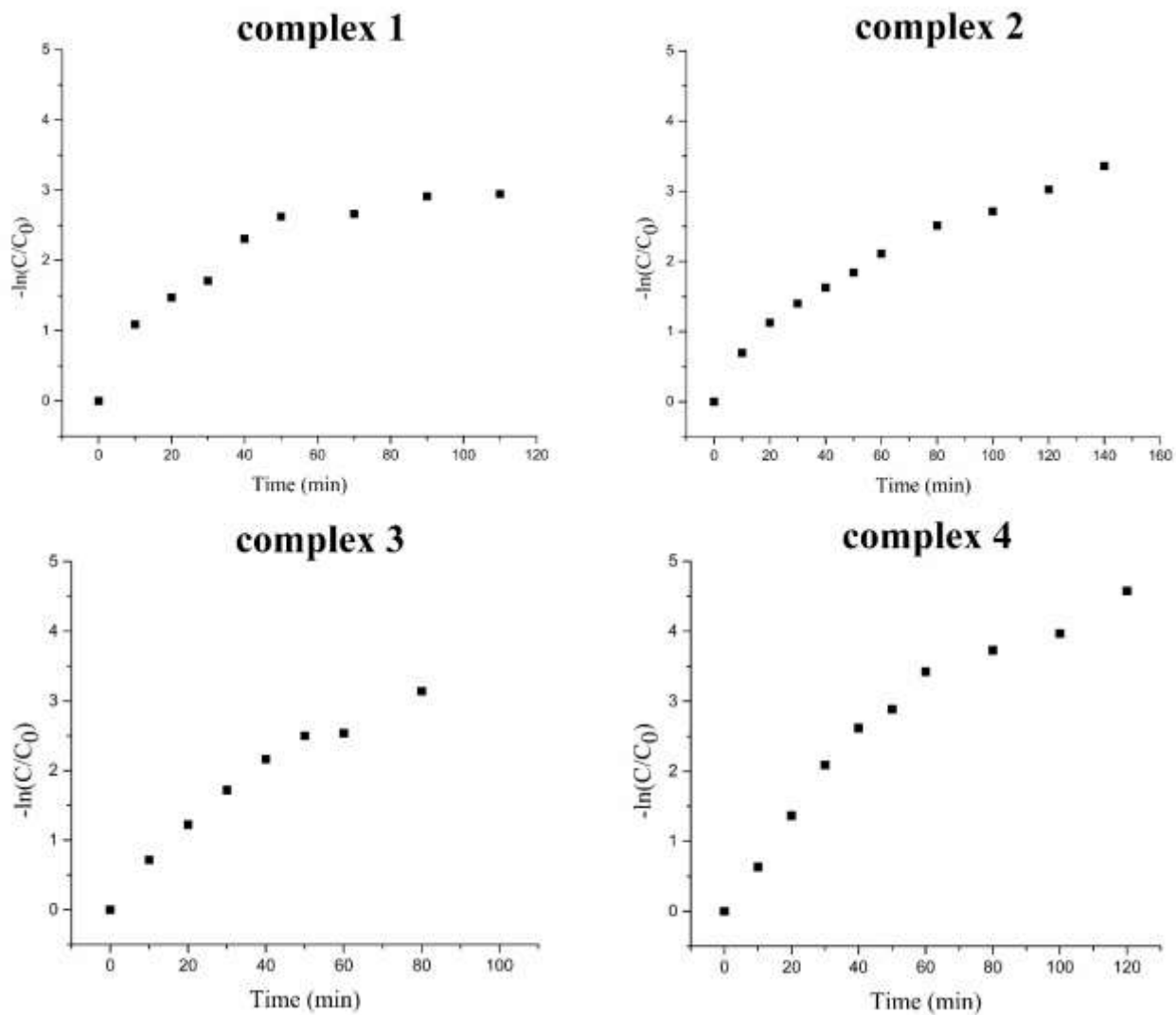| Complex	Rate constant (min^{-1})
1	0.049±0.006
2	0.029±0.003
3	0.045±0.003
4	0.061±0.002

Figure 11. Dependence of −ln(C/C₀) on time for the photocatalytic degradation reaction of MB9 dye for **1–4**.
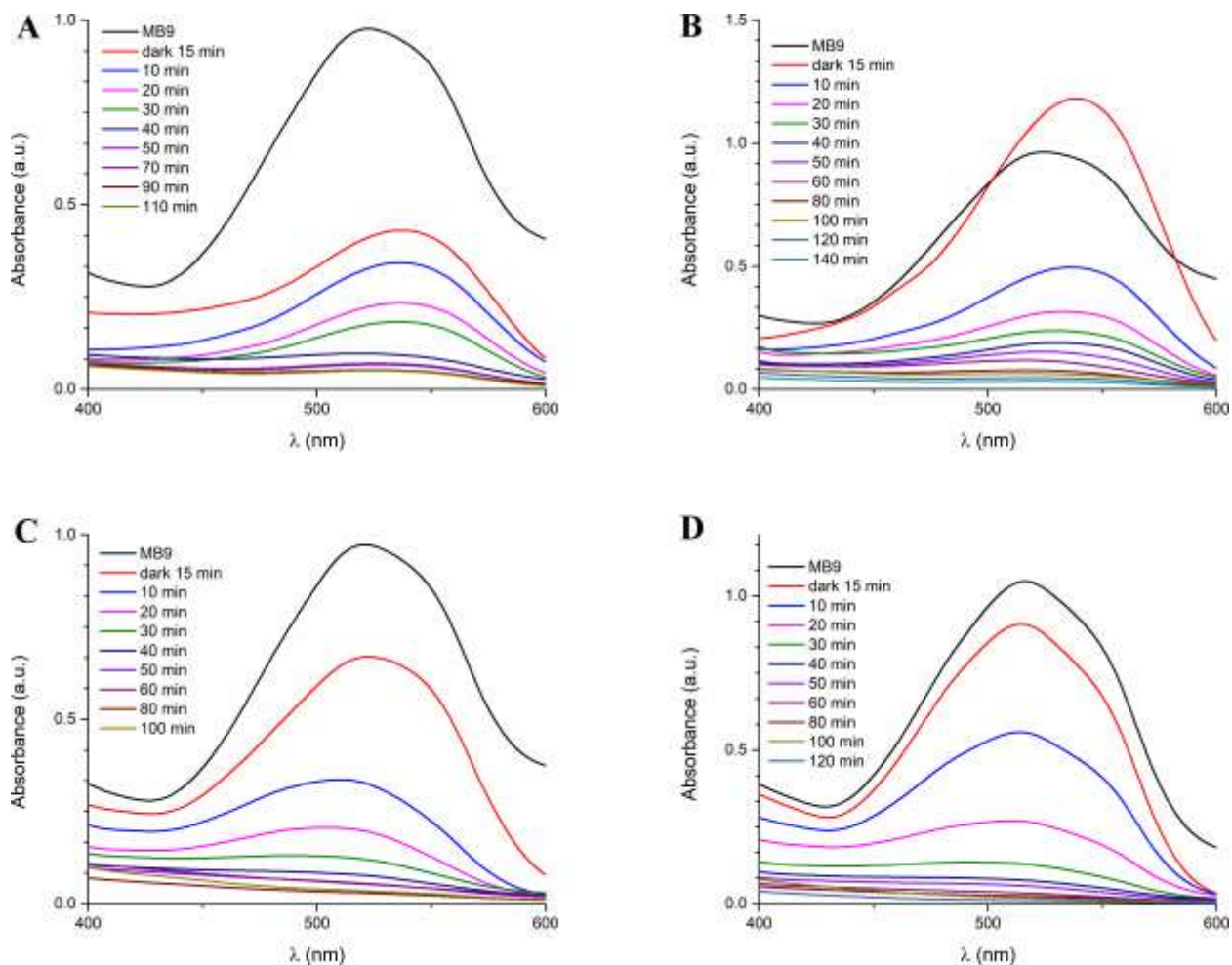
Figure 12. UV-VIS spectra showing the progress of photocatalytic degradation of MB9 dye for **1–4**.

The concentration ratios of MB9 (C_t/C_0) against irradiation time (min) in the presence of **1–4** were plotted (Figure S3), where C_t denotes a concentration of the dye after irradiation time t, while C_0 is the initial concentration of MB9 after stirring in the dark for 15 min. The results obtained in the dark showed significant adsorption (more than 30 %) of MB9 for **1** and **3**. After 60 min the dye was degraded almost completely using all CPs (more than 90 %), while Degussa p25 (titania) removed 65 % (Figure S3). Taking into account that the apparent first-order rate constant was the highest for **4** and adsorption of the dye was relatively low, this complex was selected for testing of the reusability and further exploration of the photodegradation by radical trapping experiments. The changes in photodegradation percentage of MB9 after each cycle under the same experimental conditions are shown in Figure S4. There was no significant loss of photocatalytic activity of **4** in the first two cycles, while after the third cycle there was a drop of

activity. After the third cycle, the FTIR spectrum of **4** was nearly identical to the one before the first cycle (Figure S5).

A photodegradation mechanism using semiconducting materials as heterogeneous photocatalysts can be classified as direct or indirect dye degradation, the latter being more dominant.[ref RSC Adv., 2014, 4, 37003] The indirect photodegradation of organic dyes usually occurs by the formation of reactive species such as superoxide radicals ($^{\bullet}O_2^{-}$), hydroxyl radicals ($^{\bullet}OH$), photoexcited electrons, and holes (h^+).[ref RSC Adv., 2014, 4, 37003] Thus, radical trapping experiments were conducted to check the possible active species formation during the MB9 degradation process photocatalyzed by **4**. Ethyl alcohol (EtOH), benzoquinone (BQ), or ammonium oxalate (AO) were introduced in the reaction system as quenchers of $^{\bullet}OH$, $^{\bullet}O_2^{-}$ and h^+, respectively (Figure S6).[ref Cryst. Growth Des. 2020, 20, 1130−1138] The results showed that all the quenchers had negligible influence on the photocatalytic activity of **4**, implying that $^{\bullet}OH$, $^{\bullet}O_2^{-}$ and h^+ are not the intermediate species, and that none of the mechanisms associated with them apply to this reaction. Therefore, since a direct degradation mechanism is less likely in a system like this, it is most likely that the degradation occurs through creation of photoexcited electrons.

Thermal characterization of 1–4

For compounds with potential applicability, it is crucial to determine their thermal stability and thermal properties in the planned applications' temperature range.[56–59] Discussed compounds represent two pairs of coordination polymers with analogue structures – **1** and **2**, and **3** and **4**, respectively. Figure 13 shows the TG and DTG curves of all four complexes. During the samples' thermal treatment in the first step, the evaporation of the solvent is expected. TG and DTG curves in Figure 13 show that only compound **3** contains a solvent which, according to single crystal X-ray diffraction (SCXRD) data, is water. The amount of water determined by TG is higher ($\Delta m = 5.2$ %) than that determined by SCXRD ($\Delta m = 3.92$ %). This means that compound **3** is hygroscopic. The DTG curve of **3** shows two peaks before 180 °C, and the mass loss is continuous. The origin of the DTG peak at 154 °C cannot be explained without the simultaneously recorded MS data. In compounds **2** and **4**, the mass loss to 150 °C is less than 0.5 %, indicating a negligible amount of adsorbed water from the air, while 1 shows no solvent traces. After evaporation of adsorbed water, compounds **2** and **4** are stable with decomposition onset temperatures of 179 and 266 °C, respectively. As the decomposition of **3** is continuous,

before practical application, it would be necessary to test its stability using isothermal measurements.

Since the cation of **1** and **2** is the same, and their structures are similar (Figure 1), the different thermal stabilities and different decomposition mechanisms are caused by the different anions, NO_3^- (**1**) and ClO_4^- (**2**). The nitrate compound is less stable. A similar trend is actual for compounds **3** and **4**: the nitrate compound's decomposition starts at a significantly lower temperature (~170 °C) than the perchlorate compound (TG onset: 266 °C, see Figure 13).

Both anions are strong oxidizing agents. The corresponding DSC curves better present the effect of oxidation with their exothermic peak temperatures, as shown in Figure 14. In the nitrate compounds, the exothermic peaks show up at 221 °C (**1**) and 213 °C (**3**), while for the perchlorate compounds, they are at 275 °C (**2**) and 294 °C (**4**). As only compound **3** contains water molecules, the sharp endothermic peak at 170 °C may indicate its melting, followed by decomposition.
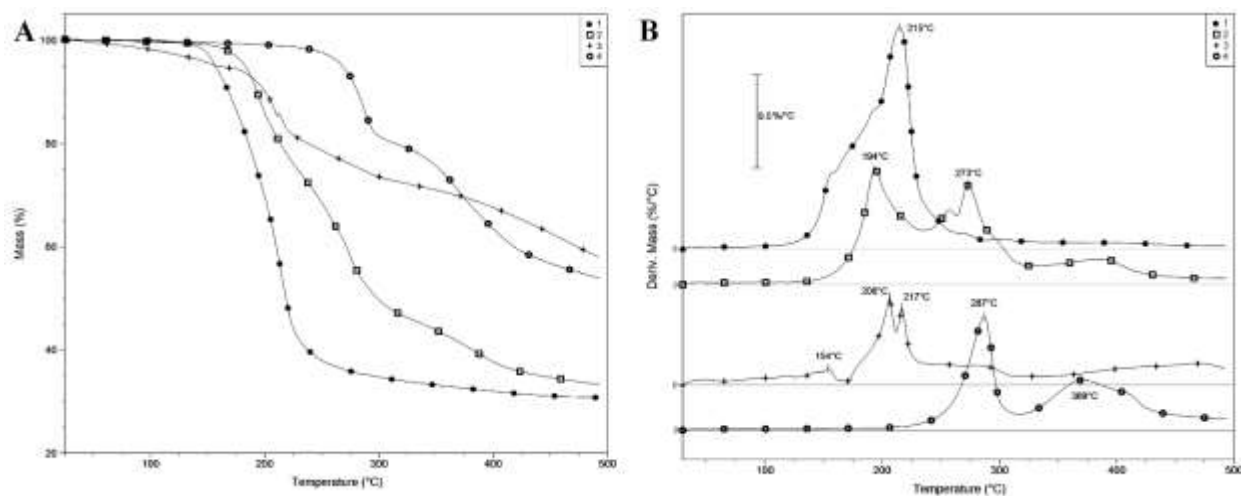

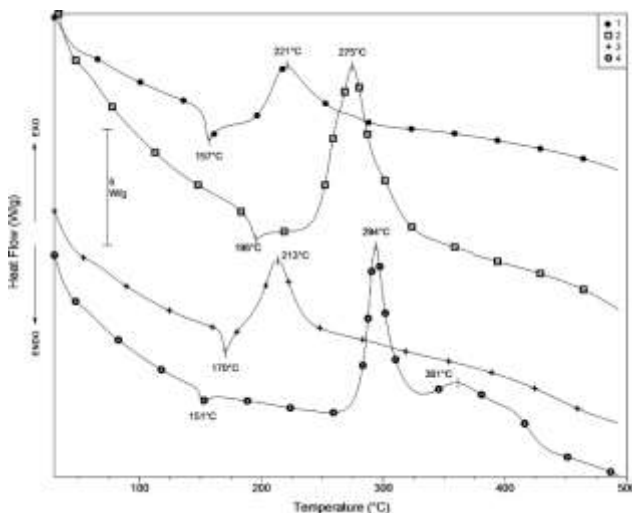Figure 13. TG (A) and DTG (B) curves of the CPs **1–4**.

Figure 14. DSC curves of compounds **1–4** in N_2.

The decomposition mechanism was studied by coupled TGA-MS measurements. Since the coordinated ligands L1 and L2 consist of C, N, H, and S (only L1) (Figures 1 and 3), their thermal decomposition products can be H^+, C^+, N^+, N_2^+ and S^+ (m/z = 1, 12, 14, 28 and 32, respectively). The only fragment detected in all four spectra is N^+, but the peak for N_2^+ is missing (Figure 15a). The TG-MS curves in Figure 15A show the evolution of a fragment with $m/z = 14$ in all CPs in the temperature range of 120 – 200 °C, which may indicate the scission of a nitrogen atom of the ligand, thus resulting in the partial destruction of the polymeric structure of all four complexes. Namely, it is implausible that the fragment is related to the evolution of CH_2^+, requiring the scission of the N–CH$_2$ bond of the ring. Interestingly fragment $m/z = 14$ was detected in the case of **4** at ~150 °C, too. Due to the lower sensitivity of TG measurements, the corresponding mass loss was not detected. Only a small endothermic DSC peak can be attributed to the process (see Figure 15B). The only reasonable explanation of this peak's appearance could be the scission of one of the nitrogen atoms from the terminal NH groups, which are not stabilized by inter- or intramolecular interactions. In **1** and **2**, the evolution of S^+ is detected at 226 °C (**1**) and 271 °C (**2**), which is in accordance with the structure of the ligand. Other possible fragments of L1 and L2 are CN^+, HCN^+, and $C_2H_2N^+$ (m/z = 26, 27 and 40, respectively), but the last one cannot be identified because it has the same molar mass as argon used as a purge gas. Fragments with m/z = 26 and 27, which, besides CN^+ and HCN^+, may belong to ring fragments ($C_2H_2^+$ and $C_2H_3^+$), were detected only in **2** and **4**.
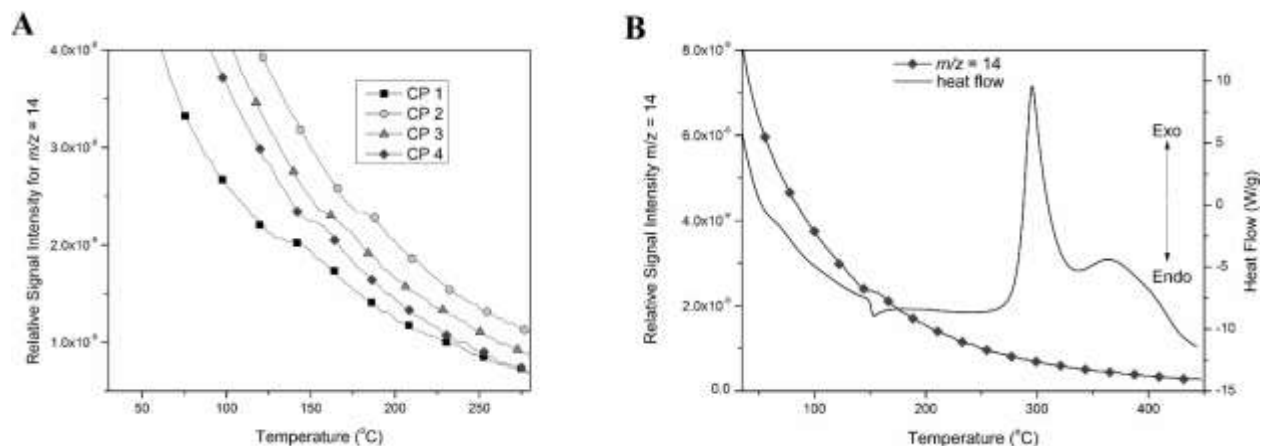
Figure 15. DSC curves of *m/z* = 14 in all four compounds (A); Curve of **4** and its signal for *m/z* = 14 (B).

Since all CPs contain highly oxidative anions, intramolecular redox reactions and their products are expected in the form of H_2O, CO or/and CO_2 and nitrogen oxides. All these signals' intensity was monitored in all the compounds (see Figures 16 and 17). The evolution of the signals at *m/z* = 18 and 17 characteristic for water (Figure 16) at the beginning of the heating program show that all the compounds absorbed small amounts of water during the storage, which evaporates from room temperature. Peaks of *m/z* 18 and 17 during the decomposition of CPs with the fragments of *m/z* = 44 (CO_2 or N_2O) are the results of the oxidation of the ligands L1 and L2 due to the anion. Also, **1** and **2** due to sulfur content of L1 give fragments of SO and SO_2 with *m/z* = 48 and 64, respectively, detected at ~300 °C. MS curves of **2** are presented in Figure 18. The signal *m/z* = 36 detected in perchlorate compounds (**2** and **4**) most probably belongs to evolved HCl. Its intensity increased with increasing temperature (Figure 19).
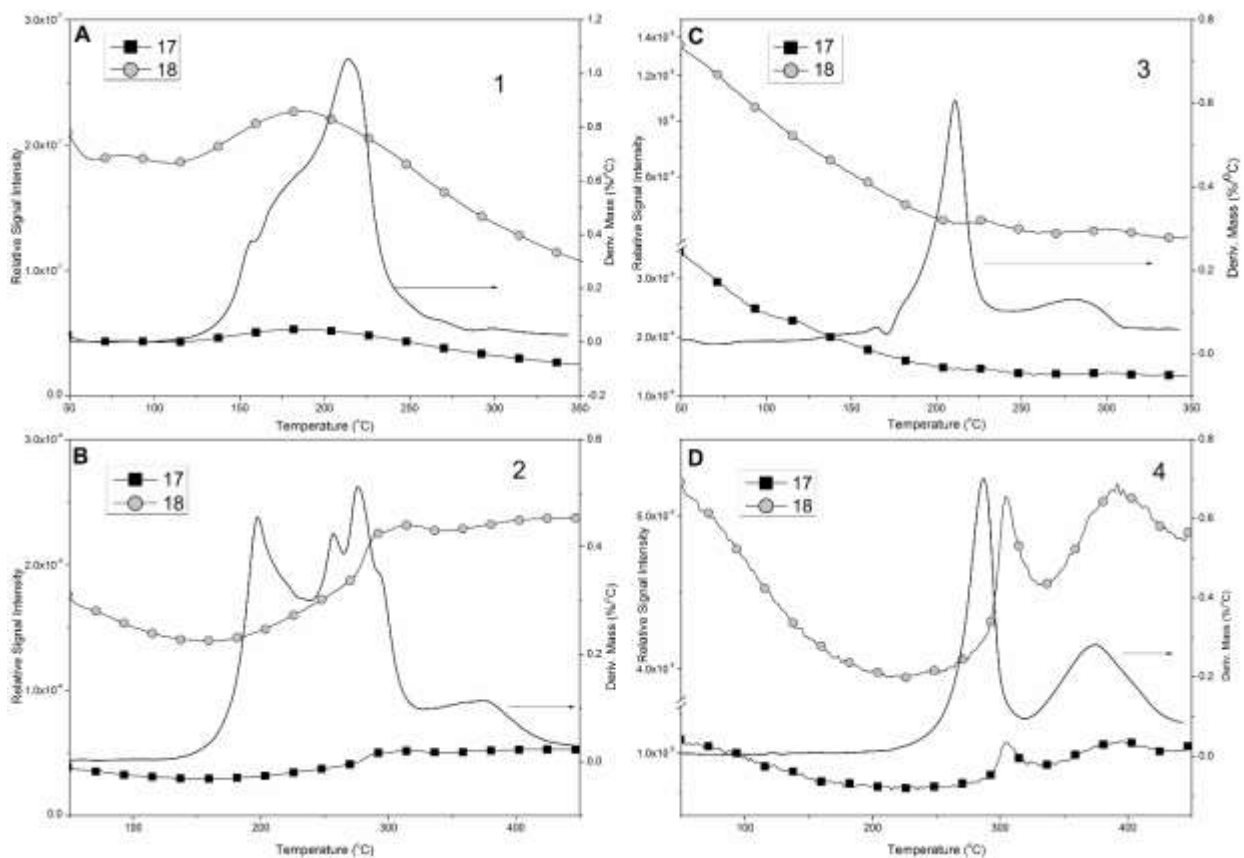
29

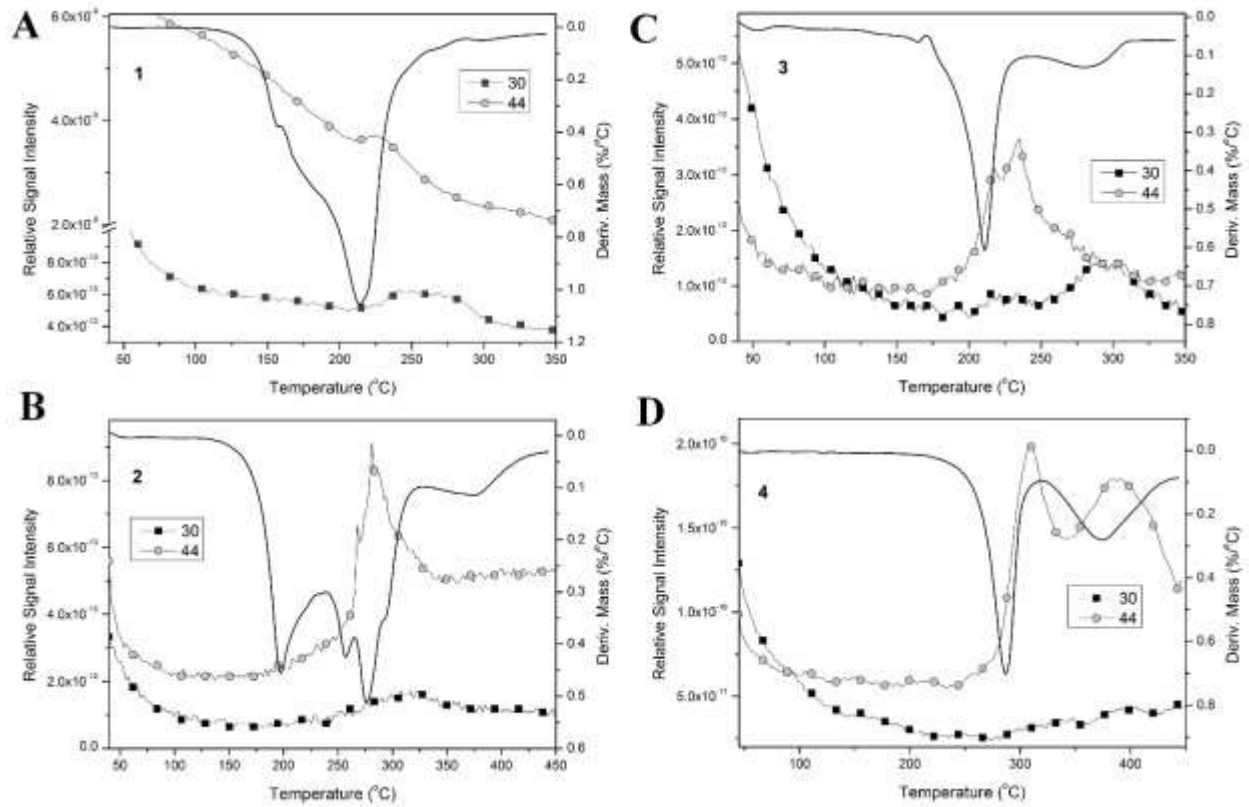Figure 16. Peaks of water evaporation from **1** (A), **2** (B), **3** (C), and **4** (D).

Fugure 17. Peaks of NO and CO$_2$ or N$_2$O (m/z = 30 and 44) evaporation from **1** (A), **2** (B), **3** (C) and **4** (D).
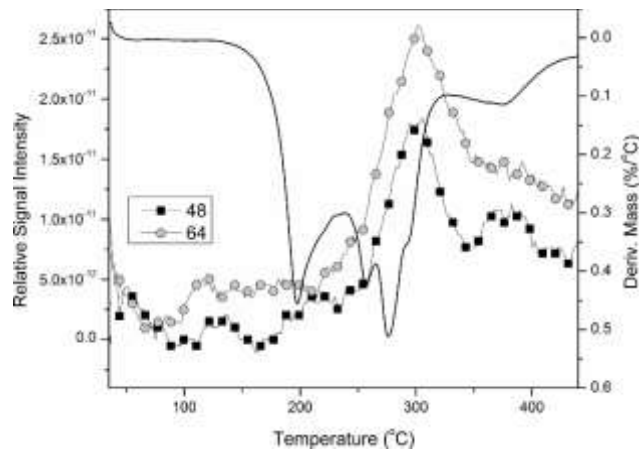

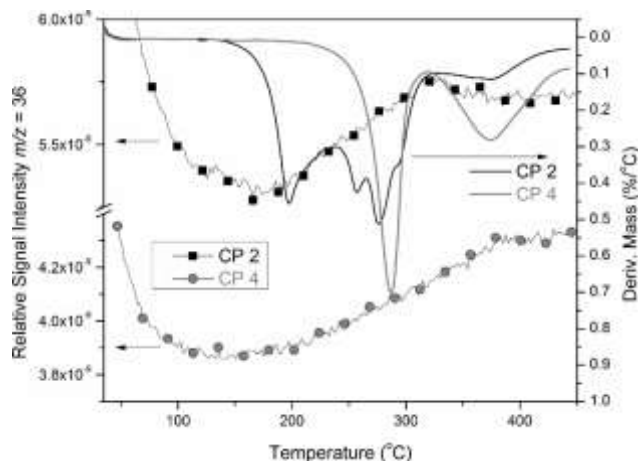Figure 18. Peaks of SO and SO$_2$ evolution (m/z = 48 (SO$^+$) and 64 (SO$_2^+$)) of **2**.

Figure 19. Peaks for *m/z* = 36 of CPs **2** and **4**.

Conclusion

Four new Ag(I) coordination polymers with thiomorpholine-4-carbonitrile (L1) and piperazine-1,4-dicarbonitrile ligands (L2) were synthesized and characterized. Compounds **1** and **2** crystallize in the tetragonal $P\bar{4}2_1m$ space group, while **3** and **4** crystallize in the triclinic $P\bar{1}$ and orthorhombic *Pnnn* space groups, respectively. In all four structures, L1 and L2 behave as 1,4-*bis*-monodentate ligands, while the Ag(I) ion is four coordinated in a slightly distorted geometry. Topological analysis in standard representations suggests that each Ag(I) atom in **1–4** acts as a 4-connected node, and the structures **1** and **2** have **sql**, while **3** and **4** have **dia** underlying net topology. Thermal analysis showed a trend in thermal stability where **1** and **3** (NO_3^- based) have lower onset temperatures (150 ˚C and r.t.) than **2** and **4** (ClO_4^- based; 179 and 266 ˚C), which indicates the influence of the oxidizing ability of the anions on thermal stability. Photocatalytic properties were measured for the photocatalytic degradation of MB 9 dye and show that all compounds exhibit good reaction rates, superior to Degussa titania powder. The results are correlated with the size and compactness of the unit cell.

Accession Codes

CCDC 2068533-2068536 contain the supplementary crystallographic data for this paper. These data can be obtained free of charge via www.ccdc.cam.ac.uk/data_request/cif or by emailing

data_request@ccdc.cam.ac.uk, or by contacting The Cambridge Crystallographic Data Centre, 12 Union Road, Cambridge CB2 1EZ, UK; fax: +44 1223 336033.

Conflicts of interest

There are no conflicts of interest to declare.

Acknowledgments

References

1   F. X. Coudert and A. H. Fuchs, *Coord. Chem. Rev.*, 2016, **307**, 211–236.

2   K. Vellingiri, A. Deep and K. H. Kim, *ACS Appl. Mater. Interfaces*, 2016, **8**, 29835–29857.

3   J. A. Cruz-Navarro, F. Hernandez-Garcia and G. A. Alvarez Romero, *Coord. Chem. Rev.*, 2020, **412**, 213263.

4   P. Rocío-Bautista, I. Taima-Mancera, J. Pasán and V. Pino, *Separations*, 2019, **6**, 1–21.

5   C. Pettinari, F. Marchetti, N. Mosca, G. Tosi and A. Drozdov, *Polym. Int.*, 2017, **66**, 731–744.

6   M. Berchel, S. Hernot, H. Couthon-Gourvès, J. P. Haelters, F. Quentel, T. Le Gall, T. Montier, P. Lehn, G. B. Hix, O. Pérez, J. M. Rueff and P. A. Jaffrès, *Phosphorus, Sulfur Silicon Relat. Elem.*, 2013, **188**, 76–78.

7   R. J. Young, S. L. Begg, C. J. Coghlan, C. A. McDevitt and C. J. Sumby, *Eur. J. Inorg. Chem.*, 2018, **2018**, 3512–3518.

8   G. Wang, T. Chen, X. Wang, H. Ma and H. Pang, *Eur. J. Inorg. Chem.*, 2017, **2017**, 5350–5355.

9   M. S. Chen, Z. Su, M. Chen, S. S. Chen, Y. Z. Li and W. Y. Sun, *CrystEngComm*, 2010, **12**, 3267–3276.

10   G. X. Liu, X. M. Ren, H. Xu, S. Nishihara and R. Y. Huang, *Inorg. Chem. Commun.*, 2009, **12**, 895–897.

11   Y. Li, J. D. An, T. T. Wang, Q. Wang, Y. H. Qiao and B. Ding, *Inorg. Nano-Metal Chem.*, 2020, **0**, 1–9.

12   C. R. Groom, I. J. Bruno, M. P. Lightfoot and S. C. Ward, *Acta Crystallogr. Sect. B Struct. Sci. Cryst. Eng. Mater.*, 2016, **72**, 171–179.

13   P. Ristić, T. R. Todorović, V. Blagojević, O. R. Klisurić, I. Marjanović, B. B. Holló, P. Vulić, M. Gulea, M. Donnard, M. Monge, M. Rodríguez-Castillo, J. M. López-De-Luzuriaga and N. R. Filipović, *Cryst. Growth Des.*, 2020, **20**, 4461–4478.

14   S. Y. Hao, Y. H. Li, Z. C. Hao and G. H. Cui, *Ultrason. Sonochem.*, 2017, **39**, 636–644.

15   X. Yue Cheng, R. Qing Miao, Q. Qi Zhou, T. Zhang, D. Feng Wang and R. Bin Huang, *Inorg. Chem. Commun.*, 2018, **90**, 15–21.

16   J. Cheng, G. H. Wang and Y. W. Wang, *J. Struct. Chem.*, 2018, **59**, 729–732.

17   J.-X. Li, Z.-B. Qin, Y.-H. Li and G.-H. Cui, *Ultrason. Sonochem.*, 2018, **48**, 127–135.

18   J.-N. X. and T.-Y. S. Jia-Yin Sun, Li Wang, Dao-Jun Zhang, Da Li, Yu Cao, Li-Ying Zhang, Shuang-Li Zeng, Guang-Sheng Pang, Yong Fan, *CrystEngComm*, 2013, **15**, 3402–3411.

19   D. Huang, X. Wu, J. Tian, X. Wang, Z. Zhou and D. Li, *Chinese Chem. Lett.*, 2018, **29**, 845–848.

20   L. Zhang, X. Kuang, X. Wu, W. Yang and C. Lu, *Dalt. Trans.*, 2014, **43**, 7146–7152.

21   H. N. Chang, L. W. Liu, Z. C. Hao and G. H. Cui, *J. Mol. Struct.*, 2018, **1155**, 496–502.

22   X. Q. Wu, G. X. Wen, Y. P. Wu, W. W. Dong, J. Zhao and D. S. Li, *J. Solid State Chem.*,

2016, **242**, 243–247.

23　C. P. Ye, G. Xu, Z. Wang, J. Han, L. Xue, F. Y. Cao, Q. Zhang, L. F. Yang, L. Z. Lin and X. D. Chen, *Dalt. Trans.*, 2018, **47**, 6470–6478.

24　X. Tan, X. Chen, J. Zhang and C. Y. Su, *Dalt. Trans.*, 2012, **41**, 3616–3619.

25　M. Y. Masoomi and A. Morsali, *Coord. Chem. Rev.*, 2012, **256**, 2921–2943.

26　C. Shen, Y. G. Xu and M. Lu, *J. Mater. Chem. A*, 2017, **5**, 18854–18861.

27　C. P. Li, H. Zhou, J. J. Wang, B. L. Liu, S. Wang, X. Yang, Z. L. Wang, C. Sen Liu, M. Du and W. Zhou, *ACS Appl. Mater. Interfaces*, 2019, **11**, 42375–42384.

28　S. Mandal, S. P. Nanavati, D. J. Willock and R. Ananthakrishnan, *J. Phys. Chem. C*, 2019, **123**, 23940–23950.

29　G. Kumar, S. Pandey and R. Gupta, *Cryst. Growth Des.*, 2018, **18**, 5501–5511.

30　M. I. Rogovoy, A. S. Berezin, Y. N. Kozlova, D. G. Samsonenko and A. V. Artemev, *Inorg. Chem. Commun.*, 2019, **108**, 107513.

31　N. I. Sulaiman, N. R. Salimin, R. A. Haque, M. A. Iqbal, S. W. Ng and M. R. Razali, *Polyhedron*, 2015, **97**, 188–196.

32　H. Huang, M. Payehghadr, J. Wang, H. P. Xiao, A. Y. Wang, X. H. Li and A. Morsali, *Helv. Chim. Acta*, 2014, **97**, 345–354.

33　S. Roy, H. M. Titi, B. K. Tripuramallu, N. Bhunia, R. Verma and I. Goldberg, *Cryst. Growth Des.*, 2016, **16**, 2814–2825.

34　D. Sun, G. G. Luo, N. Zhang, Q. J. Xu, C. F. Yang, Z. H. Wei, Y. C. Jin, L. R. Lin, R. Bin Huang and L. S. Zheng, *Inorg. Chem. Commun.*, 2010, **13**, 290–293.

35　H. He, S. Q. Wang, Z. Y. Han, X. H. Tian, W. W. Zhang, C. P. Li and M. Du, *Appl. Surf. Sci.*, 2020, **531**, 147342.

36　CrysAlis PRO, Rigaku Oxford diffraction Ltd: Yarnton, Oxfordshire, 2021.

37　R. C. Clark and J. S. Reid, *Acta Crystallogr. Sect. A*, 1995, **51**, 887–897.

38   G. M. Sheldrick, *Acta Crystallogr. Sect. A Found. Crystallogr.*, 2015, **71**, 3–8.

39   G. M. Sheldrick, *Acta Crystallogr. Sect. C Struct. Chem.*, 2015, **71**, 3–8.

40   I. J. Bruno, J. C. Cole, P. R. Edgington, M. Kessler, C. F. Macrae, P. McCabe, J. Pearson and R. Taylor, *Acta Crystallogr. Sect. B Struct. Sci.*, 2002, **58**, 389–397.

41   L. J. Farrugia, *J. Appl. Crystallogr.*, 1999, **32**, 837–838.

42   E. V. Alexandrov, V. A. Blatov, A. V. Kochetkov and D. M. Proserpio, *CrystEngComm*, 2011, **13**, 3947–3958.

43   D. J. and M. A. S. Joshua J. McKinnon, *Chem. Commun.*, 2007, **37**, 3814–3816.

44   M. A. S. and A. S. M. Joshua J. McKinnon, *Acta Crystallogr. Sect. B*, 2004, **B60**, 627–668.

45   M. J. Frisch, G. W. Trucks, H. B. Schlegel, G. E. Scuseria, M. A. Robb, J. R. Cheeseman, G. Scalmani, V. Barone, G. A. Petersson, H. Nakatsuji, X. Li, M. Caricato, A. Marenich, J. Bloino, B. G. Janesko, R. Gomperts, B. Mennucci, H. P. Hratchian, J. V. Ortiz, A. F. Izmaylov, J. L. Sonnenberg, D. Williams-Young, F. Ding, F. Lipparini, F. Egidi, J. Goings, B. Peng, A. Petrone, T. Henderson, D. Ranasinghe, V. G. Zakrzewski, J. Gao, N. Rega, G. Zheng, W. Liang, M. Hada, M. Ehara, K. Toyota, R. Fukuda, J. Hasegawa, M. Ishida, T. Nakajima, Y. Honda, O. Kitao, H. Nakai, T. Vreven, K. Throssell, J. A. Jr. Montgomery, J. E. Peralta, F. Ogliaro, M. Bearpark, J. J. Heyd, E. Brothers, K. N. Kudin, V. N. Staroverov, T. Keith, R. Kobayashi, J. Normand, K. Raghavachari, A. Rendell, J. C. Burant, S. S. Iyengar, J. Tomasi, M. Cossi, J. M. Millam, M. Klene, C. Adamo, R. Cammi, J. W. Ochterski, R. L. Martin, K. Morokuma, O. Farkas, J. B. Foresman, D. J. Fox, Gaussian 09, Revision A.02, Gaussian, Inc., Wallingford CT, 2009.

46   K. V. Kumar, K. Porkodi and F. Rocha, *Catal. Commun.*, 2008, **9**, 82–84.

47   D. R. P. and R. P. H. Lei Yang, *Dalt. Trans.*, 2007, **9**, 955–964.

48   I. A. Baburin, V. A. Blatov, L. Carlucci, G. Ciani and D. M. Proserpio, *J. Solid State Chem.*, 2005, **178**, 2452–2474.

49   T. Maity, H. Mandal, A. Bauzá, B. C. Samanta, A. Frontera and S. K. Seth, *New J. Chem.*,

2018, **42**, 10202–10213.

50   M. A. Spackman and J. J. McKinnon, *CrystEngComm*, 2002, **4**, 378–392.

51   X. M. Li, Z. T. Wang, V. Valtchev, Q. R. Fang and Y. R. Pan, *J. Chem. Crystallogr.*, 2020, **50**, 155–163.

52   J. X. Li, Z. Bin Qin, Y. H. Li and G. H. Cui, *Ultrason. Sonochem.*, 2018, **48**, 127–135.

53   X. X. Lu, Y. H. Luo, C. Lu, X. Chen and H. Zhang, *J. Solid State Chem.*, 2015, **232**, 123–130.

54   J. C. Geng, L. Qin, X. Du, S. L. Xiao and G. H. Cui, *Zeitschrift fur Anorg. und Allg. Chemie*, 2012, **638**, 1233–1238.

55   Y. Y. Yang, L. X. Zhou, Y. Q. Zheng, H. L. Zhu and W. Y. Li, *J. Solid State Chem.*, 2017, **253**, 211–218.

56   F. Farhadi Abkanar, A. Eslami and M. Kubicki, *J. Therm. Anal. Calorim.*, 2020, **140**, 1779–1789.

57   J. Magyari, B. Barta Holló, L. S. Vojinović-Ješić, M. M. Radanović, S. Armaković, S. J. Armaković, J. Molnár, A. Kincses, M. Gajdács, G. Spengler and K. Meszaros Szecsenyi, *New J. Chem.*, 2018, **42**, 5834–5843.

58   B. Barta Holló, L. S. Vojinović Ješić, M. M. Radanović, M. V. Rodić, Ž. K. Jaćimović and K. Mészáros Szécsényi, *J. Therm. Anal. Calorim.*, 2020, **142**, 451–460.

59   B. Holló, M. V. Rodić, L. S. Vojinović-Ješić, V. Živković-Radovanović, G. Vučković, V. M. Leovac and K. M. Szécsényi, *J. Therm. Anal. Calorim.*, 2014, **116**, 655–662.

Graphical abstract

2D and 3D Silver-Based Coordination Polymers with Thiomorpholine-4-carbonitrile and Piperazine-1,4-dicarbonitrile: Structure, Intermolecular Interactions, Photocatalysis, and Thermal Behavior

Predrag Ristić, Nenad Filipović, Vladimir Blagojević, Jovana Ćirković, Berta Barta Holló, Morgan Donnard, Mihaela Gulea, Ivana Marjanović, Olivera R. Klisurić, Tamara R. Todorović

The reaction of thiomorpholine-4-carbonitrile and piperazine-1,4-dicarbonitrile ligands afforded four Ag(I) coordination polymers with excellent photocatalytic activity in the degradation of mordant blue 9 dye.